New Evidence for a Physical Link between Asteroids (155140) 2005 UD and (3200) Phaethon

Maxime Devogèle, Eric Maclennan, Annika Gustafsson, Nicholas Moskovitz, Joey Chatelain, Galin Borisov, Shinsuke Abe, Tomoko Arai, Grigori Fedorets, Marin Ferrais, et al.

The Planetary Science Journal, 1:15 (15pp), 2020 June https://doi.org/10.3847/PSJ/ab8e45

New Evidence for a Physical Link between Asteroids (155140) 2005 UD and (3200) Phaethon*

Maxime Devogèle[1], Eric MacLennan[2], Annika Gustafsson[3], Nicholas Moskovitz[1], Joey Chatelain[4], Galin Borisov[5,6], Shinsuke Abe[7], Tomoko Arai[8], Grigori Fedorets[2,9], Marin Ferrais[10,11,12], Mikael Granvik[2,13], Emmanuel Jehin[10], Lauri Siltala[2,14], Mikko Pöntinen[2], Michael Mommert[1], David Polishook[15], Brian Skiff[1], Paolo Tanga[16], and Fumi Yoshida[8]
[1] Lowell Observatory, 1400 W. Mars Hill Rd., Flagstaff, AZ 86001, USA; mdevogele@lowell.edu
[2] Department of Physics, P.O. Box 64, FI-00014 University of Helsinki, Finland
[3] Department of Astronomy & Planetary Science, Northern Arizona University, P.O. Box 6010, Flagstaff, AZ 86011, USA
[4] Las Cumbres Observatory, CA, USA
[5] Armagh Observatory and Planetarium, College Hill, Armagh BT61 9DG, UK
[6] Institute of Astronomy and National Astronomical Observatory, Bulgarian Academy of Sciences, 72, Tsarigradsko Chaussèe Blvd., Sofia BG-1784, Bulgaria
[7] Aerospace Engineering, Nihon University, 7-24-1 Narashinodai, Funabashi, Chiba 2748501, Japan
[8] Planetary Exploration Research Center, Chiba Institute of Technology, Narashino, Japan
[9] Astrophysics Research Centre, School of Mathematics and Physics, Queen's University Belfast, Belfast BT7 1NN, UK
[10] Space sciences, Technologies & Astrophysics Research (STAR) Institute University of Liège Allée du 6 Août 19, B-4000 Liège, Belgium
[11] Aix Marseille Université, CNRS, LAM (Laboratoire d'Astrophysique de Marseille) UMR 7326, F-13388, Marseille, France
[12] Space sciences, Technologies, France
[13] Division of Space Technology, Luleå University of Technology, Box 848, SE-98128 Kiruna, Sweden
[14] Nordic Optical Telescope, Apartado 474, E-38700 S/C de La Palma, Santa Cruz de Tenerife, Spain
[15] Faculty of Physics, Weizmann Institute of Science, 234 Herzl St. Rehovot 7610001, Israel
[16] Université Côte d'Azur, Observatoire de la Côte d'Azur, CNRS, Laboratoire Lagrange, Boulevard de l'Observatoire, CS34229, F-06304 Nice Cedex 4, France
Received 2020 January 29; revised 2020 April 25; accepted 2020 April 27; published 2020 May 20

Abstract

In 2018, the near-Earth object (155140) 2005 UD (hereafter UD) experienced a close fly by of the Earth. We present results from an observational campaign involving photometric, spectroscopic, and polarimetric observations carried out across a wide range of phase angles (0°.7–88°). We also analyze archival NEOWISE observations. We report an absolute magnitude of $H_V = 17.51 \pm 0.02$ mag and an albedo of $p_V = 0.10 \pm 0.02$. UD has been dynamically linked to Phaethon due their similar orbital configurations. Assuming similar surface properties, we derived new estimates for the diameters of Phaethon and UD of $D = 5.4 \pm 0.5$ km and $D = 1.3 \pm 0.1$ km, respectively. Thermophysical modeling of NEOWISE data suggests a surface thermal inertia of $\Gamma = 300^{+120}_{-110}$ and regolith grain size in the range of 0.9–10 mm for UD and grain sizes of 3–30 mm for Phaethon. The light curve of UD displays a symmetric shape with a reduced amplitude of $Am(0) = 0.29$ mag and increasing at a linear rate of 0.017 mag/° between phase angles of 0° and ~25°. Little variation in light-curve morphology was observed throughout the apparition. Using light-curve inversion techniques, we obtained a sidereal rotation period $P = 5.235 \pm 0.005$ hr. A search for rotational variation in spectroscopic and polarimetric properties yielded negative results within observational uncertainties of ~10% μm^{-1} and ~16%, respectively. In this work, we present new evidence that Phaethon and UD are similar in composition and surface properties, strengthening the arguments for a genetic relationship between these two objects.

Unified Astronomy Thesaurus concepts: Near-Earth objects (1092); CCD observation (207); Astronomical techniques (1684); Photometry (1234); Polarimetry (1278); Spectroscopy (1558)

1. Introduction

The Apollo-type near-Earth object (NEO; 155140) 2005 UD (hereafter UD) was discovered by the Catalina Sky Survey in 2005 (Christensen et al. 2005, MPEC 2005-U22). Ohtsuka et al. (2006) and Jewitt & Hsieh (2006) showed that it displays orbital properties and photometric colors similar to the well-known NEO (3200) Phaethon, suggesting a genetic relationship between the two. However, more recent dynamical analyses have raised questions regarding a formal link (Ryabova et al. 2019), though the chaotic nature of orbits in near-Earth space suggests that any dynamical correlation between the two bodies would not be maintained for more than a few thousand years (Schunová et al. 2014).

(3200) Phaethon is an intriguing NEO both in terms of orbital elements and physical properties. It displays a highly eccentric orbit ($e = 0.89$) associated with a very low perihelion distance ($q = 0.14$ au). Its close approaches to the Sun suggest that its surface experiences large diurnal and seasonal temperature variations. Phaethon has also been linked to the Geminid meteor stream (Whipple 1983; Ryabova 2012). However, very low levels of activity centered on just a few days around perihelion are too low to explain the observed Geminid meteor flux (Li & Jewitt 2013). Phaethon is also considered to be the parent of three other meteor streams, all belonging to the Geminid meteor complex. These streams correspond to the intersection of the orbit of the Earth with that of Phaethon's at different epochs (Babadzhanov & Obrubov 1987; Jakubík & Neslušan 2015). However, one of these

* Partially based on data collected with 2 m RCC telescope at Rozhen National Astronomical Observatory.

Table 1
Osculating Orbital Elements of Phaethon and Its Two Companions 2005 UD and 1999 YC at Epoch 59,000.0 MJD Obtained with the JPL Horizons Service

	Phaethon	2005 UD	1999 YC
a (au)	1.271	1.275	1.422
e	0.890	0.872	0.831
i (°)	22.259	28.668	38.232
ω (°)	265.2	19.7	64.8
Ω (°)	322.2	207.6	156.4

streams, the daytime Sextantids, seems to be more closely related to UD than it is to Phaethon (Ohtsuka et al. 2005, 2006).

Phaethon and UD are also dynamically associated with another asteroid, (225416) 1999 YC (Kasuga & Jewitt 2008, hereafter YC). However, while Phaethon and UD display photometric colors and spectra indicative of a blue slope and a B-type spectral classification, YC shows redder colors more consistent with a C-type classification (Kasuga & Jewitt 2008). Table 1 compares the orbital elements of the parent body Phaethon with its two putative family members UD and YC. Though the current osculating orbital elements of Phaethon and UD are different, particularly the longitude of ascending node and the argument of perihelion angles, they display similar secular variations in orbital elements with a time lag $\Delta t \sim 4600$ yr (Ohtsuka et al. 2006). This means that ~4600 yr ago, the orbital elements of Phaethon were similar to those of UD today. In the case of YC, the semimajor axis is significantly different from that of Phaethon and UD. If YC is genetically related to Phaethon and UD, these differences can only be explained if the orbit of YC was perturbed during a close planetary encounter (Ohtsuka et al. 2008). If these three asteroids are actually related, their formation mechanism is unclear and could involve YORP spin-up and fission (Pravec et al. 2010), impacts with other asteroids, or thermally driven separation during a perihelion passage (Granvik et al. 2016).

Phaethon has been the subject of many studies to understand its physical properties. The exact size and albedo of Phaethon remains uncertain as different techniques provide different results. Estimates for the albedo range from 0.075 to 0.16 (Hanuš et al. 2016, 2018; Ito et al. 2018; Shinnaka et al. 2018; Zheltobryukhov et al. 2018; Masiero et al. 2019). This wide range in geometric albedo implies a wide range of possible diameters. Based on thermophysical modeling (TPM), Hanuš et al. (2018, 2016) reported an albedo of $p_v = 0.122 \pm 0.008$, giving an associated volume-equivalent diameter of $D = 5.1 \pm 0.2$ km, while Masiero et al. (2019) reported an albedo of $p_v = 0.16 \pm 0.02$ and a diameter of $D = 4.6^{+0.2}_{-0.3}$ km. On the other hand, Kareta et al. (2018) used the short-wavelength tail of the thermal emission obtained from near-infrared spectroscopy and derived an average visible albedo of $p_v = 0.08 \pm 0.01$. Moreover, polarimetric measurements of Phaethon show a very high degree of linear polarization (maximum polarization $P_{max} \sim 45\%$) characteristic of low-albedo B-type asteroids (Devogèle et al. 2018; Ito et al. 2018; Shinnaka et al. 2018; Zheltobryukhov et al. 2018), thus, implying a larger size. During a near-Earth fly by in 2017, Phaethon was observed using radar at the Arecibo Observatory (Taylor et al. 2019). These observations revealed an equatorial diameter ranging from 6.1 to 6.4 km depending on rotational phase. Lastly, stellar occultation data of Phaethon from 2019 (Dunham et al. 2019) revealed a diameter more consistent with $D \sim 5$ km. These discrepancies in albedo and size could result from Phaethon having an uncommon or inhomogeneous surface. Variation of the linear degree of polarization was indeed observed as a function of the rotation phase suggesting that the surface of Phaethon is not uniform (Borisov et al. 2018; Devogèle et al. 2018).

The spectrum of Phaethon displays a blue slope compatible with a B-type taxonomy in the Bus and Binzel (visible; Bus & Binzel 2002) and Bus-DeMeo (NIR inclusive; DeMeo et al. 2009) systems. Spectral variation with rotation was found by Kareta et al. (2018), however, with marginal significance.

Phaethon is the target of the Japanese Aerospace Exploration Agency's Demonstration and Experiment of Space Technology for INterplanetary voYage Phaethon fLyby dUSt science (DESTINY$^+$) mission. It is planned to launch in 2022 and will perform a high-speed fly by of Phaethon (Arai et al. 2018). A possible mission extension for DESTINY$^+$ would be a fly by of UD. As a result, ground-based campaigns of telescopic observations focused on both objects have been organized for mission preparation purposes. In this work, we present photometric, spectroscopic, and polarimetric results for UD and discuss its relation with its suspected parent body, Phaethon.

In the next section, we present a summary of our observations of UD in photometry, spectroscopy, and polarimetry. We also detail the thermal data used from NEOWISE. For each technique, the data acquisition and reduction procedures are detailed. Section 3 is devoted to discussion of the results from each technique. From the photometry, we discuss the rotation period and pole determination of UD. As our observations span a large range of phase angles, we also determined the photometric phase curve, estimation of the absolute H magnitude, size of UD, and the variation of the amplitude as a function of the phase angle. The visible spectroscopy allowed us to determine the taxonomic type of UD and compare it with the spectrum of Phaethon. Polarimetric observations allowed for characterization of the phase-polarization curve of UD and also for comparison to Phaethon. An estimate of the albedo was obtained using the albedo–polarization relation (Cellino et al. 2015). From the TPM, we derive the thermal inertia of UD and the expected size of the regolith particles on its surface. We also obtain another estimation of its size and albedo. Finally, a search for surface inhomogeneities was performed by analyzing spectral and polarimetric variations as a function of rotational phase. Section 4 is devoted to the discussion of the results and comparison with Phaethon, while the last section is devoted to the conclusions.

2. Observations and Data Reduction

We obtained photometric, spectroscopic, and polarimetric observations of 2005 UD during its favorable 2018 apparition when it reached a minimum geocentric distance of $\Delta = 0.223$ au on September 28 and a minimum apparent magnitude of $V = 15.7$ mag on October 12. This apparition was the best opportunity to observe it until 2041, when it will fly by the Earth at a distance of $\Delta = 0.092$ au and reach $V = 14.1$ mag. UD will make a closer approach to the Earth in 2028 October ($\Delta = 0.217$ au), although its V magnitude will not be brighter than $V = 17.1$ mag.

Table 2
Summary of Photometric Observations Presented in This Work

UT Date	JD −2,458,000.0	MPC	V (mag)	Exp. (s)	α (deg)	Δ (au)	r (au)
2018 Sep 27	388.52	K92	16.4	15	58	0.22	1.10
2018 Sep 27	388.79	688	16.4	180	57	0.22	1.11
2018 Sep 27	389.19	Q63	16.4	15	55	0.22	1.11
2018 Oct 1	393.16	Q63	16.1	30	38	0.23	1.17
2018 Oct 2	393.48	K92	16.0	30	36	0.23	1.18
2018 Oct 3	394.73	W86	16.0	35	31	0.23	1.19
2018 Oct 4	395.49	K92	15.9	30	28	0.24	1.20
2018 Oct 6	397.62	I40	15.9	50	20	0.25	1.24
2018 Oct 6	397.67	688	15.9	120	20	0.25	1.23
2018 Oct 9	401.07	Q63	15.8	30	9	0.29	1.28
2018 Oct 9	401.35	K92	15.8	30	8	0.29	1.28
2018 Oct 10	401.50	Z53	15.8	50	7	0.29	1.29
2018 Oct 10	401.65	688	15.8	120	7	0.29	1.29
2018 Oct 10	401.70	W86	15.8	30	7	0.29	1.29
2018 Oct 13	404.71	W86	15.7	30	0.7	0.33	1.33
2018 Oct 13	405.00	Q63	15.7	30	1	0.33	1.33
2018 Oct 14	406.01	Q63	16.0	30	3	0.35	1.34
2018 Oct 15	406.60	688	16.2	120	4	0.36	1.35
2018 Oct 15	407.30	K92	16.2	35	6	0.37	1.36
2018 Oct 16	407.58	W86	16.4	35	6	0.37	1.36
2018 Oct 16	407.60	688	16.4	120	6	0.37	1.36
2018 Oct 16	408.01	Q63	16.4	35	7	0.38	1.37
2018 Oct 16	408.33	K92	16.4	40	7	0.38	1.37
2018 Oct 17	408.62	I40	16.6	50	8	0.39	1.38
2018 Oct 17	408.68	W86	16.6	40	8	0.39	1.38
2018 Oct 19	411.49	I40	16.9	50	11	0.43	1.41
2018 Oct 20	411.57	W86	17.1	50	12	0.43	1.41
2018 Oct 25	416.93	Q63	17.7	80	18	0.52	1.47
2018 Oct 27	418.57	W86	18.0	90	20	0.55	1.49
2018 Oct 28	419.50	W86	18.1	100	20	0.56	1.50
2018 Oct 30	421.94	Q63	18.3	120	22	0.61	1.53
2018 Oct 31	422.93	097	18.4	180	23	0.64	1.54
2018 Oct 31	423.16	Q63	18.4	130	23	0.63	1.54
2018 Nov 1	423.57	W86	18.5	120	23	0.64	1.55
2018 Nov 1	424.16	097	18.5	180	24	0.65	1.55
2018 Nov 2	424.61	W86	18.6	120	24	0.66	1.56

Note. JD corresponds to the Julian date minus 2,458,000.0, MPC stands for the Minor Planet Center code, V corresponds to the magnitude in the V filter according to the Minor Planet Center Search Results Web results ephemeris service, and α, Δ, and r correspond to the light-curve mean phase angle and UD distance to Earth and the Sun, respectively.

2.1. Photometry

We observed UD photometrically in 36 different sessions throughout the 2018 apparition. We used the Las Cumbres Observatory (LCO) network of robotic 1 m telescopes. Six different LCO telescopes from three sites—Cerro Tololo Inter-American Observatory (Minor Planet Center (MPC) observatory code W86), South African Astronomical Observatory (K92), and Siding Springs Observatory (Q63)—were used. We also used the 0.71 m telescope from Wise Observatory in the Negev desert in Israel (097), Lowell Observatory's 0.7 m robotic telescope (688) located on Anderson Mesa in Northern Arizona, and the TRAPPIST-South (I40) and TRAPPIST-North (Z53) telescopes (Jehin et al. 2011) located at la Silla Observatory (Chile) and Oukaimeden Observatory (Morocco). Observations were conducted from 2018 September 27 to November 2 allowing us to probe phase angles ranging from 0°.7 to 58°. All sessions are detailed in Table 2.

At the LCO 1 m telescopes, the Sinistro instruments were employed. Sinistro captures a 26′ field, sampled at a pixel scale of 0.″389 pixel^{-1}. Images were obtained using the LCO Pan-STARRS w filter, which provides broad uniform transmission from 0.4 to 0.85 μm. All images were reduced by the LCO pipeline using standard bias and flat field corrections.

At the Wise observatory, the observations were performed using the 0.71 m telescope, equipped with an FLI ProLine PL16801 CCD, providing a 4096 × 4096 pixels and a field of view of 57′ × 57′ (Brosch et al. 2015).

At the Lowell 0.7 m, the NASA31 CCD (a 2k × 2k e2v CCD) was used to capture a 15.′7 field of view, sampled at a pixel scale of 0.″45 pixel^{-1}. Images were obtained using a broadband Cousins R filter. All images were reduced using standard bias and flat field correction techniques.

Both TRAPPIST telescopes are 0.6 m robotic Ritchey–Chrétien designs operating at $f/8$ on German Equatorial mounts. At TRAPPIST-North, the camera is an Andor IKONL BEX2 DD (0.″60 pixel^{-1}, 20 × 20′ field of view), and at TRAPPIST-South, it is an FLI ProLine 3041-BB (0.″64 pixel^{-1}, 22 × 22′ field of view). Images were obtained on

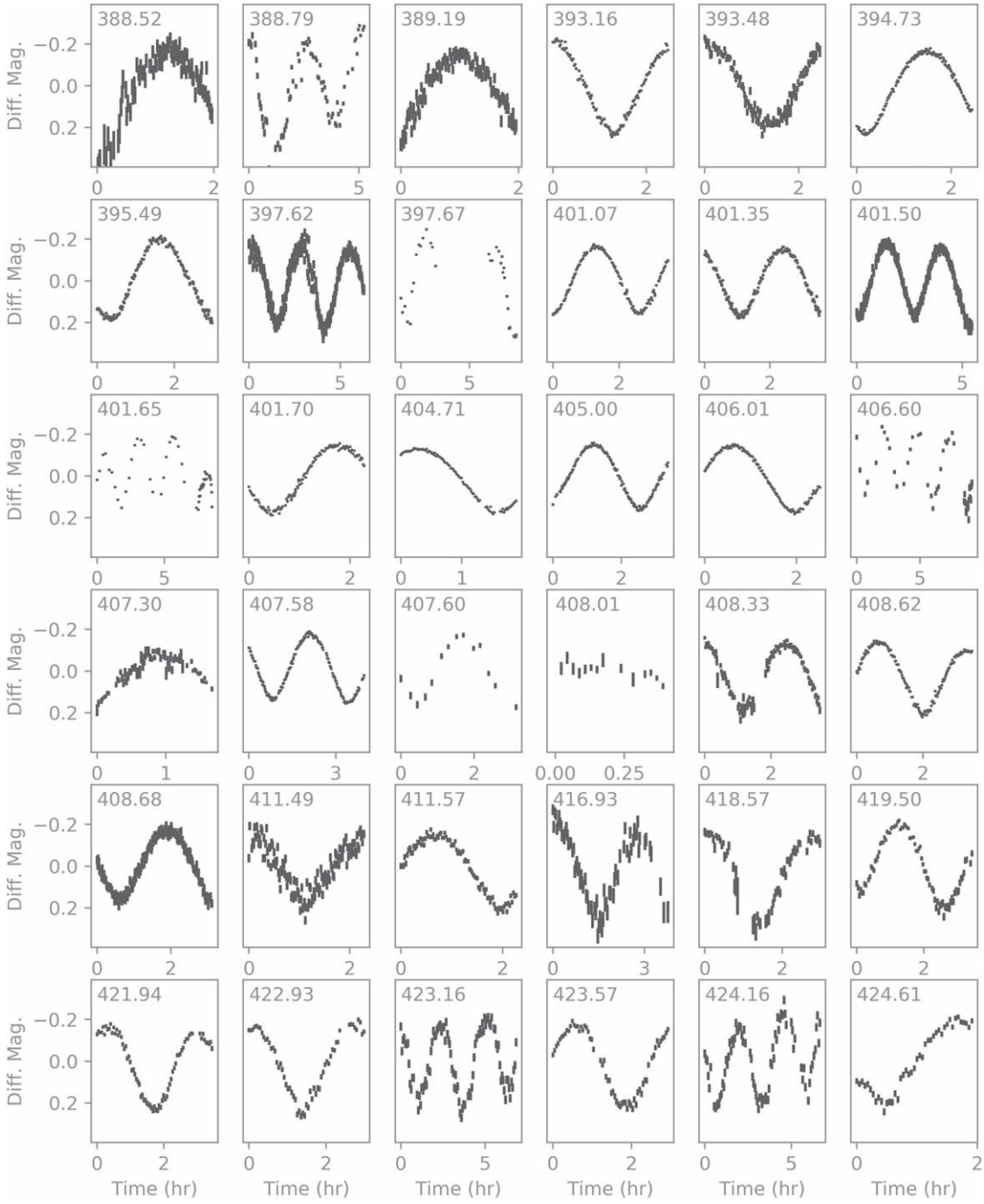

Figure 1. The full suite of differential light-curve photometry of UD collected during the 2018 apparition. Julian dates—2,458,000.0 at the beginning of each observing session are shown in the upper left corner of each sub-plot.

both telescopes with a binning of 2 × 2 and a broadband Johnson Cousins *R* filter.

All photometry from LCO, TRAPPIST, and the Lowell observatory were measured using the PHOTOMETRYPIPELINE (Mommert 2017). The photometric zero-point was obtained for each image by referencing the r' magnitudes of on-chip field stars (typically ∼100 per image) in the Pan-STARRS catalog. The Wise observatory data were reduced using standard procedures as described in Polishook & Brosch (2009).

The full ensemble of light curves is shown in Figure 1.

2.2. Polarimetry

Polarimetric observations were obtained from two facilities: the 2 m telescope at BNAO-Rozhen Observatory (071) in Bulgaria using the 2-Channel-Focal-Reducer Rozhen (FoReRo2; Jockers et al. 2000) and the 2.5 m Nordic Optical Telescope (NOT; Z23) at the Observatorio del Roque de los Muchachos, La Palma, Canary Islands, Spain using the ALFOSC instrument with the FAPOL polarimeter. For both instruments, the polarization measurements were performed by inserting a retarder half-wave plate and a Wollaston prism (FoReRo2) or

a calcite plate (FAPOL) in the optical path. The half-wave retarder plate rotates the orientation of the incident electric field before the Wollaston or calcite plate by steps of 45° (by rotating the retarder by steps of 22.°5) and by using the beam swapping technique, described in Bagnulo et al. (2006), accurately measure the q and u Stokes parameters (Shurcliff 1962) and, thus, the linear polarization of the observed source. The main difference between FoReRo2 and the FAPOL polarimeter is the use of a field mask, to avoid superposition of the two beams, in the case of the FoReRo2 instrument.

The linear degree of polarization of solar system objects is usually expressed with the P_r parameter. This parameter corresponds to the flux difference between the scattered sunlight that has an electric wave oscillating in the planes perpendicular and parallel to the scattering plane (plane containing the Sun, the object, and the observer), normalized to their sum, as follows:

$$P_r = \frac{I_{//} - I\perp}{I_{//} + I\perp}. \quad (1)$$

Details on how to derive P_r with instruments similar to FoReRo2 and FAPOL are provided in Bagnulo et al. (2006).

The polarimetric observations were carried out on October 2, 4, and 6 at Rozhen and on September 18, 20, and 30 and October 4, 5, 6, 11, 12, 14, 15, and 17 at the NOT. Table 3 lists all of the individual polarization measurements of UD. During the first two Rozhen nights, UD was continuously observed over 6 hr, allowing us to cover more than one rotational period (assuming $P = 5.235$ hr) to probe for variation of the linear polarization with respect to rotation phase. On the other hand, in the case of the NOT, multiple observations have been combined to increase the accuracy of the P_r determination. The phase angle varied from 87.°71 to 0.°74 during the observational period, allowing us to analyze the phase-polarization curve in great detail and compare it to that of (3200) Phaethon.

2.3. Spectroscopy

Visible spectroscopic observations were obtained at the Southern Astrophysical Research Telescope (SOAR) 4.1 m telescope (I11) located on the Cerro Parchón summit in Chile at an altitude of 2738 m on 2018 October 19 and 20. The Goodman Spectrograph with the red camera, grating of 400 lines per mm, and a slit width of 3.″2 was used. The red camera provides an optimal response for wavelengths longer than 0.4 μm and displays minimal fringing at the reddest wavelengths. The 400 lines per mm grating allow for spectral observation from 0.5 to 0.9 μm. A slit width of 3.″2 was used to minimize slit loss and time lost due to target (re-)acquisition. This combination of grating and slit width provided a resolution of $R \sim 400$. On each night, UD was observed continuously over a period of time slightly longer than the presumed five hour rotation period. However, the observations of UD were regularly interrupted by calibration exposures of the solar analog star SA 115–271 (for solar spectrum removal and correction of telluric absorption lines) and arc lamp exposures for wavelength calibration. Biases and flat fields were acquired at the beginning of each night. Solar analog and arcs lamp observations were obtained every 45 minutes to account for variations in airmass and atmospheric conditions. Standard spectroscopic reduction procedures were applied to all individual observations as described in Devogèle et al. (2019).

During both nights, a total of 60 individual exposures of 180 s were acquired. During the first night, observations were acquired from 00:41 to 06:56 UT, while UD had a $V = 16.9$ mag and varied in airmass from 1.71 to 2.03 with a minimum of 1.25 at 03:26 UT. During the second night, observations were acquired between 00:50 and 06:45 UT with airmass ranging from 1.59 to 2.16 with a minimum of 1.25 at 03:17 UT and $V = 17.1$ mag.

2.4. Thermophysical Modeling of WISE Data

The NEOWISE reactivation mission (NEOWISE-R; Mainzer et al. 2014) observed UD on two separate occasions. The short-wavelength filters (W1: 3.4 μm and W2: 4.6 μm) were used during these observations. These NEOWISE-R observations of UD occurred when it was 1.36 and 1.03 au from the Sun and at large solar phase angles ($\alpha = 45°$ and 76°) before and after opposition. Thus, the thermal inertia, along with diameter and albedo, can be determined through use of a thermophysical model (TPM). Here, we detail the observations and describe the approach taken to model the thermophysical properties of UD.

Moving objects observed with NEOWISE-R are detected with WMOPS (Mainzer et al. 2011) and reported to the MPC, where the information regarding the sky position and time of observation can be retrieved. The Infrared Processing and Analysis Center[17] (IPAC) houses the extracted photometric data. In downloading the data, we used the MPC observation file to parse the WISE All-Sky Single Exposure (L1b) catalog on IPAC's Infrared Science Archive (IRSA) and select detections acquired within 10 s of that reported to the MPC and within a search cone of 10″. We shift the isophotal wavelengths of the filters as per the recommendation of the WISE Explanatory supplement (Cutri 2012). Since the criteria used to parse IPAC can potentially return unwanted (non-asteroidal) or contaminated (i.e., by a background star or galaxy) infrared sources from the catalog, we employ Peirce's Criterion (Peirce 1852; Gould 1855) on the infrared color, W2–W1, as detailed in MacLennan & Emery (2018), to exclude the observations of asteroids contaminated by background sources that have different color–temperatures. These criteria left us with six and three observations in both W1 and W2 for each epoch, or 18 data points in total. During the fitting procedure, we perform a color-correction to the model fluxes to account for the fact that asteroid blackbody temperatures are drastically different than those used for calibration (Wright et al. 2010).

The thermal emission for UD is modeled by first calculating surface temperatures for a rotating spherical object and later mapping those temperatures to a prolate ellipsoid with axis ratio of $a/b = 1.45$. This approach is the same as that presented in MacLennan & Emery (2018) and is briefly reviewed here. Unlike that work, which uses the WISE observations at mid-infrared wavelengths, we use the shortwave infrared WISE bands of asteroids, for which we must account for a non-negligible contribution of reflected sunlight. Thus, we describe the way in which we account for reflected light after describing our TPM and thermal flux calculation below.

Our TPM numerically solves the one-dimensional heat transfer equation (Fourier's Law) using the estimated insolation (incoming solar radiation) as the energy input. The discrete facets are characterized as planar faces and divided into latitude bins. We calculate surface temperatures over a diurnal cycle by

[17] http://irsa.ipac.caltech.edu/Missions/wise.html

Table 3
Polarimetric Observations Presented in This Work

UT Date	JD −2458000.0	V (mag)	α (deg)	Δ (au)	r (au)	P_r (%)	Facility
2018 Sep 18	380.706 9	17.7	87.71	0.28	0.96	31.92 ± 0.78	NOT
2018 Sep 29	391.720 0	16.2	44.03	0.22	1.13	8.73 ± 0.30	NOT
2018 Sep 30	392.744 3	16.2	39.52	0.22	1.15	6.23 ± 0.06	NOT
2018 Oct 1	393.628 8	16.1	35.73	0.23	1.16	5.03 ± 0.06	NOT
2018 Oct 2	394.396 0	16.0	32.51	0.23	1.18	3.62 ± 0.07	Rozhen
2018 Oct 2	394.407 7	16.0	32.46	0.23	1.18	4.04 ± 0.08	Rozhen
2018 Oct 2	394.427 5	16.0	32.37	0.23	1.18	3.77 ± 0.07	Rozhen
2018 Oct 2	394.439 3	16.0	32.32	0.23	1.18	3.04 ± 0.07	Rozhen
2018 Oct 2	394.459 8	16.0	32.24	0.23	1.18	3.56 ± 0.13	Rozhen
2018 Oct 2	394.471 8	16.0	32.19	0.23	1.18	3.64 ± 0.13	Rozhen
2018 Oct 3	394.502 2	16.0	32.06	0.23	1.18	3.70 ± 0.13	Rozhen
2018 Oct 3	394.524 8	16.0	31.97	0.23	1.18	3.53 ± 0.13	Rozhen
2018 Oct 3	394.536 5	16.0	31.92	0.23	1.18	3.85 ± 0.15	Rozhen
2018 Oct 3	394.556 4	16.0	31.83	0.23	1.18	3.28 ± 0.15	Rozhen
2018 Oct 3	394.568 1	16.0	31.79	0.23	1.18	3.28 ± 0.13	Rozhen
2018 Oct 3	394.588 9	16.0	31.70	0.23	1.18	3.59 ± 0.13	Rozhen
2018 Oct 3	394.600 4	16.0	31.65	0.23	1.18	3.48 ± 0.13	Rozhen
2018 Oct 3	394.619 7	16.0	31.57	0.23	1.18	3.11 ± 0.14	Rozhen
2018 Oct 3	394.631 2	16.0	31.52	0.23	1.18	3.66 ± 0.15	Rozhen
2018 Oct 4	396.343 8	15.9	24.73	0.24	1.20	1.16 ± 0.13	Rozhen
2018 Oct 4	396.355 7	15.9	24.68	0.24	1.20	1.31 ± 0.14	Rozhen
2018 Oct 4	396.375 9	15.9	24.61	0.24	1.20	1.13 ± 0.15	Rozhen
2018 Oct 4	396.389 2	15.9	24.56	0.24	1.20	1.09 ± 0.14	Rozhen
2018 Oct 4	396.408 9	15.9	24.48	0.24	1.20	1.27 ± 0.13	Rozhen
2018 Oct 4	396.420 7	15.9	24.43	0.24	1.20	1.20 ± 0.13	Rozhen
2018 Oct 4	396.441 1	15.9	24.36	0.24	1.20	0.83 ± 0.12	Rozhen
2018 Oct 4	396.453 1	15.9	24.31	0.24	1.20	1.02 ± 0.12	Rozhen
2018 Oct 4	396.477 0	15.9	24.22	0.24	1.20	0.95 ± 0.13	Rozhen
2018 Oct 4	396.481 7	15.9	24.20	0.24	1.20	0.76 ± 0.07	NOT
2018 Oct 4	396.489 1	15.9	24.17	0.24	1.20	0.88 ± 0.14	Rozhen
2018 Oct 5	396.509 0	15.9	24.10	0.24	1.20	0.71 ± 0.13	Rozhen
2018 Oct 5	396.521 4	15.9	24.05	0.24	1.20	0.95 ± 0.12	Rozhen
2018 Oct 5	396.544 7	15.9	23.96	0.24	1.20	0.86 ± 0.11	Rozhen
2018 Oct 5	396.556 5	15.9	23.91	0.24	1.20	0.72 ± 0.13	Rozhen
2018 Oct 5	396.577 5	15.9	23.83	0.24	1.20	0.93 ± 0.13	Rozhen
2018 Oct 5	397.460 9	15.9	20.59	0.25	1.23	0.09 ± 0.05	NOT
2018 Oct 5	397.497 1	15.9	20.46	0.25	1.23	0.14 ± 0.10	NOT
2018 Oct 6	397.537 1	15.9	20.31	0.25	1.23	0.16 ± 0.06	NOT
2018 Oct 6	397.582 7	15.9	20.14	0.25	1.23	0.10 ± 0.06	NOT
2018 Oct 6	397.633 7	15.9	19.96	0.25	1.23	0.003 ± 0.04	NOT
2018 Oct 6	398.437 8	15.9	17.15	0.25	1.23	−0.10 ± 0.17	Rozhen
2018 Oct 6	398.453 7	15.9	17.10	0.25	1.23	−0.13 ± 0.17	Rozhen
2018 Oct 11	403.493 0	15.8	2.58	0.25	1.23	−0.64 ± 0.05	NOT
2018 Oct 12	404.393 6	15.7	0.74	0.25	1.23	−0.22 ± 0.07	NOT
2018 Oct 14	405.576 6	15.9	2.25	0.25	1.23	−0.44 ± 0.07	NOT
2018 Oct 15	406.560 7	16.2	4.18	0.25	1.23	−0.95 ± 0.06	NOT
2018 Oct 17	408.610 4	16.6	7.83	0.25	1.23	−1.11 ± 0.05	NOT

Note. JD corresponds to the Julian date minus 2,458,000.0, V corresponds to the magnitude in the V filter according to the Minor Planet Center ephemeris web service, and α, Δ, and r correspond to the light-curve mean phase angle and UD distance to Earth and the Sun, respectively. The last column, P_r corresponds to the measured partial linear polarization in percent.

rotating the facets about the spin axis of the object. Two types of surfaces are modeled: a perfectly smooth surface in which only direct insolation is considered, and a rough surface that is comprised of spherical-section craters, for which direct and multiply scattered insolation and thermally re-radiated energy from other facets are calculated. We characterize surface roughness by the mean surface slope ($\bar{\theta}$; Hapke 1984), which is varied by changing both the opening angle of the crater (γ) and the proportion of surface area that is covered by those craters (f_R); the latter is implemented when calculating the flux contribution of the rough and smooth surfaces. Here, we use three distinct default roughness values: low ($\bar{\theta} = 10°$), medium ($\bar{\theta} = 29°$), and high ($\bar{\theta} = 58°$).

For each value of thermal inertia, surface roughness, and spin pole orientation, the size of the object, taken to be the diameter of the volume-equivalent sphere ($D_{\rm eff}$), is varied to minimize χ^2. The effective diameter of the model is linked to the geometric albedo (p_V) through the absolute magnitude (H_V), which reduces the number of fitted TPM parameters by one. We use the phase integral, $q = 0.009082 + 0.4061\,G_1 + 0.8092\,G_2$ (Muinonen

Table 4
Summary Table of All New Quantities Obtained in This Work for Phaethon and UD

	Phaethon	2005 UD	Sections
Photometry			
Sidereal Period		$P_{\rm sid} = 5.235 \pm 0.005$ hr	3.1
Reduced amplitude		$Am(0) = 0.29$ mag	3.4
Amplitude increase coefficient		$m = 0.017$ mag/°	3.4
Shape aspect ratio		$a/b = 1.31$	3.4
Absolute magnitude in the V filter	$H_{\rm V} = 14.2$ mag	$H_{\rm V} = 17.51 \pm 0.02$ mag	4.3, 3.3
G_1 from (H, G_1, G_2) system		$G_1 = 1.09 \pm 0.02$	3.3
G_2 from (H, G_1, G_2) system		$G_2 = -0.10 \pm 0.01$	3.3
Effective diameter	$D_{\rm eff} = 6.1 \pm 0.7$ km	$D_{\rm eff} = 1.3 \pm 0.2$ km	4.3
Spectroscopy			
Taxonomy (Bus-DeMeo)		B-type	3.6
Spectral slope		Slope $= 20 \pm 10\%$ μm^{-1}	3.9
Polarimetry			
Maximum degree of negative polarization		$P_{\rm min} = -1.2 \pm 0.1\%$	3.5
Phase where $\alpha_{\rm min}$ occurs		$\alpha_{\rm min} = 9.5 \pm 0.2$	3.5
Inversion angle		$\alpha_{\rm inv} = 20.2 \pm 0.2$	3.5
Slope at $\alpha_{\rm inv}$		$h = 0.22 \pm 0.01\%$/°	3.5
Geometric albedo[a]		$p_{\rm V} = 0.11 \pm 0.02$	4.3
Geometric albedo[a]		$p_{\rm V} = 0.09 \pm 0.02$	4.3
Thermophysical Modeling			
Thermal inertia		$\Gamma = 300^{+120}_{-110}$ J m^{-2} K^{-1} s$^{-1/2}$	3.7
Geometric albedo		$p_{\rm V} = 0.14 + -0.07$	3.7
Effective diameter		$D_{\rm eff} = 1.12^{+0.49}_{-0.21}$ km	3.7
Bond albedo		$A = 0.052 \pm 0.027$	3.7
Grain size	3–30 mm	0.9–10 mm	3.8
Occultation			
Effective diameter	$D_{\rm eff} = 5.2 \pm 0.1$ km		4.3

Notes. The details on how each individual value was obtained can be found in the section referenced in the last column.
[a] The two different albedo values are derived using two different calibrations for the albedo–polarization relation (Cellino et al. 2015).

et al. 2010), and the parameters presented in this work to convert between the model geometric albedo to bolometric Bond albedo (A) as follows: $A \approx A_V = q \times p_V$.

The contribution of reflected light in W1 and W2 is modeled in a similar fashion to that in Alí-Lagoa et al. (2013) and Rozitis et al. (2018). Using the absolute magnitude and slope parameter from this work, an estimate for the amount of reflected visible light for the viewing geometry of the thermal observations is calculated using the phase curve formulation of Muinonen et al. (2010). Instead of subtracting the reflected flux from the measured value, we divide the observed flux by the fractional contribution of reflected light. This preserves the relative amplitude of the contribution from thermal emission (Rozitis et al. 2018). The fractional contribution of reflected light was very small (2%–4%) for W2 at both epochs and was ∼45% and ∼20% for W1 in each respective epoch. Given that the W1 observations from the first epoch have a significant contamination of reflected light, we remove these from use in the TPM fitting procedure, leaving 12 data points in total.

3. Results

In this section, we present the results obtained for all of the techniques described in the previous section. Table 4 presents all of the new determinations obtained in this work sorted by technique. The details on how these quantities were obtained can be found in the text.

3.1. Rotation Period

We searched for the sidereal rotation period of UD by combining our new observations with archival data (Jewitt & Hsieh 2006; Kinoshita et al. 2007) and using the light-curve inversion method presented by Kaasalainen & Torppa (2001) and Kaasalainen et al. (2001). We made use of sparse photometry from the Lowell Observatory Near-Earth Object Survey (LONEOS) using the implementation of Hanuš et al. (2011) and Hanuš et al. (2013). All possible sidereal periods were tested from 4 to 8 hr with the time interval between two tested periods set equal to $P \pm 0.5P/\Delta T$, where ΔT corresponds to the time interval between the first and last observations (Kaasalainen 2004). For each sidereal period, the inversion software searches for the pole solution and shape model that best fits all of the available light curves. Previous estimates for the synodic rotation period of 2005 UD by Jewitt & Hsieh (2006) and Kinoshita et al. (2007) are, respectively, $P = 5.23$ hr and $P = 5.2492$ hr.

We find that the overall set of data is not yet sufficient to allow for a unique solution for the sidereal rotation period

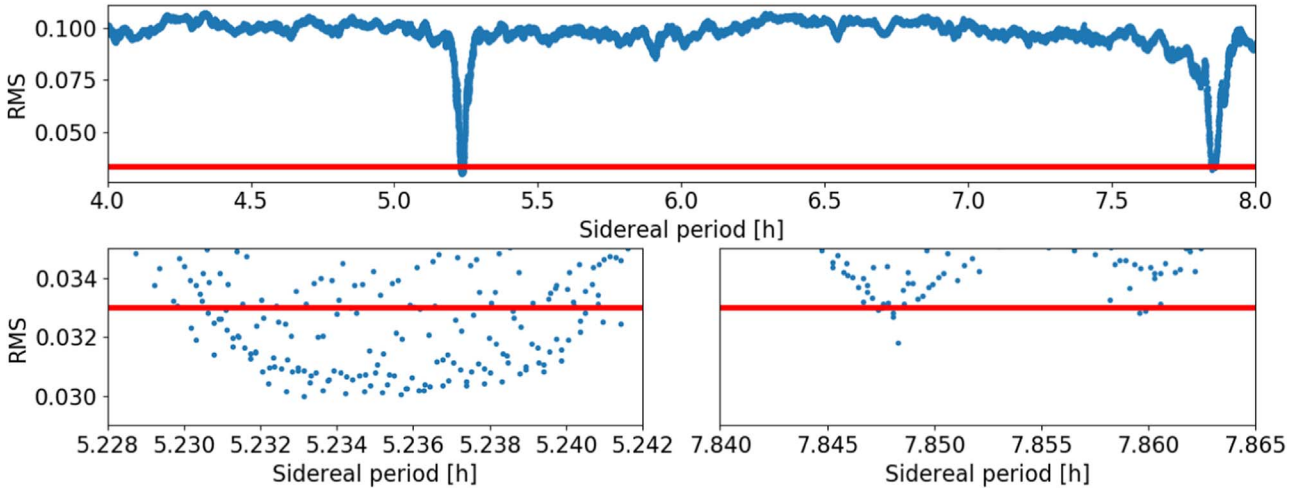

Figure 2. rms residuals for sidereal rotation periods between 4 and 8 hr obtained using the light-curve inversion method. The red line corresponds to 1.1 times the minimal residual. This threshold is used identify viable solutions. The top panel shows the whole range of tested sidereal periods while the two bottom panels zoom in on the two local minima.

(Figure 2). However, all possible solutions are contained in two narrow windows. The first, a sidereal period of $P_{\rm sid} = 5.235 \pm 0.005$ hr, is consistent with previous measurements (the sidereal period is reported here instead of the synodic period). The light curve of UD displayed a largely invariant and symmetric shape during the entire 2018 apparition (Figure 1), even though the observer phase angle varied from 0.°7 to 58°. The amplitude of the light curve is about 0.4 mag, on average, and about 0.3 mag at a minimal phase angle of ∼1°. The second statistically viable solution corresponds to a three-peaked light curve and a period around 7.84 hr. This three-peaked light-curve solution is less likely because the relatively high amplitude, ∼0.3 mag, would be inconsistent with the roughly spheroidal morphology needed to produce three peaks per revolution (Harris et al. 2014). Moreover, the inversion software provides control over the order and degree of spherical harmonics used to generate the shape models. While reducing the value of these model parameters, the rms for three-peaked solutions increases while the rms for the two-peaked solutions remains mostly unchanged. This suggests that the three-peaked solution can be excluded, and thus, we will only consider the first solution, $P_{\rm sid} = 5.235 \pm 0.005$ hr, as viable.

3.2. Pole Orientation

We search for the pole orientation of UD using both optical and thermal observations. Neither technique provided a unique pole solution, but they did provide consistent constraints on pole orientation (Figure 3).

In the case of the optical data, the light-curve inversion algorithm provides a determination of the spin-axis parameters. Even if no unique solution for the sidereal period can be found, which in turn precludes a unique solution for the pole orientation, we can still obtain physically meaningful constraints. These constraints were obtained by computing shape solutions for a set of 10,000 randomly selected initial conditions for the spin state parameters (sidereal rotation period and pole orientation). The sidereal rotation period was randomly selected between 5.230 and 5.242 hr. The pole orientation was randomly chosen with equal probability for any orientation. An rms value for each of these prescribed periods

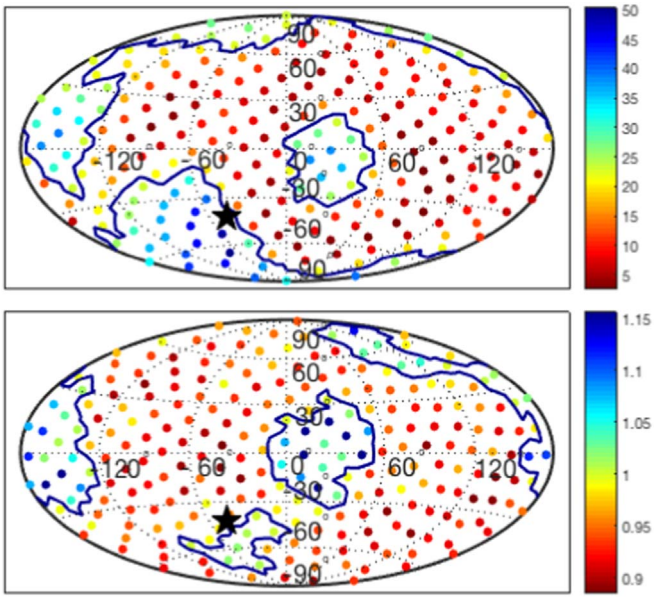

Figure 3. χ^2 of the best thermophysical (upper panel) and shape (lower panel) models as a function of the spin-axis orientation. The red dots correspond to spin orientation that are possible, while the blue dots correspond to highly improbable orientations. No preferred orientation can be determined, but some zones of the parameter space can be excluded. Both techniques (which are independent of each other) provide similar constraints. The pole orientation of Phaethon is represented by a black star in both panels.

and pole orientations was computed based on an optimized shape model.

In the case of the TPM, a search for constraints on the pole orientation was also be performed. We searched for pole solutions with NEOWISE data, using the TPM explained in Section 2.4.

With both techniques, we have a large set of shapes or thermophysical models that cover the entire phase space of spin-axis solutions. In order to constrain the orientation of the spin axis, we subdivided the celestial sphere in 250 bins of equal area and selected the model with the lowest χ^2 in each of these bins. Figure 3 presents these lowest χ^2 values. The upper panel shows the constraints obtained using TPM while the lower panel shows the constraints obtained using the shape

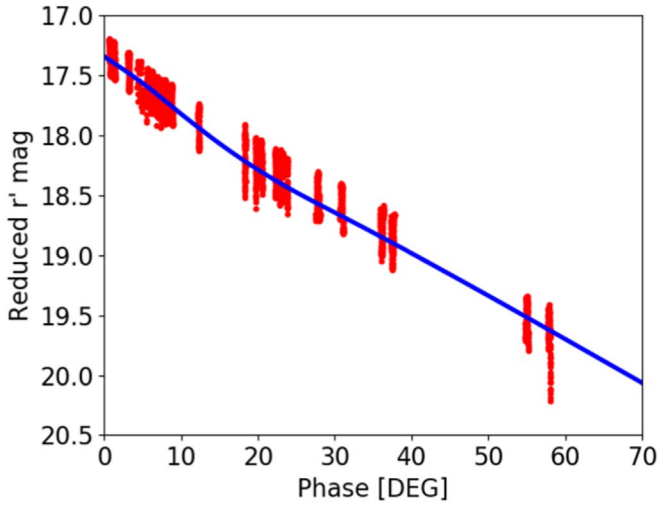

Figure 4. Photometric phase curve of 2005 UD in the r' band. The fit to the H_1, G_1, and G_2 photometric system gives $H_{r'} = 17.34 \pm 0.02$

modeling procedure. Figure 3 also displays one contour line to help distinguish areas with viable solutions (red dots) versus excluded regions (blue dots). The results show that for both independent techniques, the excluded spin-axis orientations are similar.

A pole solution similar to that of Phaethon ($\lambda = -46°$, $\beta = -47°$; black stars in Figure 3; Hanuš et al. 2018) could not be excluded but is located within an excluded region for the thermophysical model and near an excluded region for the light-curve inversion models. The most likely set of solutions shows that UD may display a pole orientation that is at least 20° different from that of Phaethon.

3.3. Photometric Phase Curve

We used the H, G_1, and G_2 photometric system (Muinonen et al. 2010) to fit the photometric phase curve of UD. The large phase angle coverage from 0.°7 to 58° allows for a precise characterization of both the nonlinear brightness surge at small phase angle ($\alpha < 7°$) and the linear part at ($\alpha > 7°$). The H, G_1, and G_2 system is defined as

$$V(\alpha) = H + 2.5 \log 10[G_1 \Phi_1(\alpha) + G_2 \Phi_2(\alpha) + (1 - G_1 - G_2)\Phi_3(\alpha)] \quad (2)$$

where $\Phi_1(\alpha)$, $\Phi_2(\alpha)$, and $\Phi_3(\alpha)$ are basis functions for which $\Phi_1(0) = \Phi_2(0) = \Phi_3(0) = 0$. Details about the H, G_1, and G_2 system can be found in Muinonen et al. (2010).

We used *python* packages from the University of Helsinki to fit our measurements of UD[18] (Penttilä et al. 2016). Figure 4 shows the photometric phase curve of UD with the best fit of the H, G_1, and G_2 model. The rotational light-curve effect is clearly seen in Figure 4 as the apparent scatter in the points at each phase angle. However, the large phase angle coverage and large number of individual data points (nearly 3000) help to average out this effect. The best fit provides $H_{r'} = 17.34 \pm 0.02$ mag, $G_1 = 1.09 \pm 0.02$, and $G_2 = -0.10 \pm 0.01$. These values are consistent with a low-albedo asteroid, as expected for a B-type asteroid (Muinonen et al. 2010). We also note that at low phase angles, there is a lack of opposition surge, which is also consistent with asteroids displaying very low albedo (Belskaya & Shevchenko 2000).

The International Astronomical Union (IAU) defines the H magnitude in the Johnson V filter. However, our observations were calibrated to the Pan-STARRS r' filter. Thus, we first convert our measurements into the Johnson R system. According to Jordi et al. (2006), we can transform r' to R magnitude using the relation $R = r'$–0.267(V–R)–0.088. We thus find $H_R = 17.16 \pm 0.02$, which is consistent with $H_R = 17.19 \pm 0.02$ reported by Jewitt & Hsieh (2006). Then, we can transform to the V filter by assuming that UD has the same V–R color as the Sun (i.e., 0.354 mag; Holmberg et al. 2006), thus, yielding $H_V = 17.51 \pm 0.02$ mag. We stress that the assumption that UD possesses the same color as the Sun is valid as the spectrum is relatively flat. Moreover, three measurements have been reported for the V–R color of UD: V–$R = 0.39$ (Kasuga & Jewitt 2008), V–$R = 0.35$ (Jewitt & Hsieh 2006), and V–$R = 0.34$ (Kinoshita et al. 2007), averaging to the color of the Sun inside our error bar for H.

3.4. Light-curve Amplitude as a Function of Phase Angle

UD displays a mostly symmetric and invariant light curve over the whole range of observations presented in this work. By fitting the light curves of UD obtained at different epochs with a sine function, we obtained a determination of its amplitude (A) as a function of phase angle. The amplitude of asteroid light curves is dependent on phase angle for several reasons. The first is purely geometrical and, for ellipsoidal shapes, shows a linear dependence with respect to phase angle for angles lower than ~30° (Zappala et al. 1990). The second factor is related to the scattering properties of the asteroid surface and was found to be dependent on the taxonomic type (Zappala et al. 1990). Using the relation described in Zappala et al. (1990) ($Am(0) = A(\alpha)/(1 - m\alpha)$), we modeled the amplitude variation of UD as a function of phase angle for angles lower than 25°. The results show that the amplitude of UD at opposition is $Am(0) = 0.29$ mag and $m = 0.017$ mag/°. This value of m is similar to those measured for low-albedo C-type asteroids (m(C) = 0.015 mag/°) but different from moderate-albedo S-type asteroids (m(S) = 0.03 mag/°; Zappala et al. 1990).

Using the relation between the amplitude of a light curve and its elongation (assuming a triaxial ellipsoid shape with $a > b > c$; $-2.5\log(a/b)$), we obtain a lower limit on the UD axis ratio $a/b = 1.34$, assuming a reduced amplitude of UD $Am(0) = 0.29$ mag.

3.5. Polarimetric Phase Curve

The phase-polarization curve of UD suggests a low-albedo asteroid with a high degree of linear polarization. This phase-polarization curve is similar to that of Phaethon, suggesting a similar albedo and optical surface properties.

Figure 5 compares the phase-polarization curves of UD and Phaethon. The results of fitting the phase-polarization curve of UD using the exponential-linear formalism (Muinonen et al. 2009) are summarized in Table 4. We found a maximum degree of negative polarization of $P_{min} = -1.2 \pm 0.1\%$ occurring at a phase angle of $\alpha_{min} = 9.°5 \pm 0.°2$ and an inversion angle $\alpha_{inv} = 20.°2 \pm 0.°2$ with a slope at inversion of $h = 0.22 \pm 0.01\%/°$.

[18] https://wiki.helsinki.fi/display/PSR/HG1G2+tools

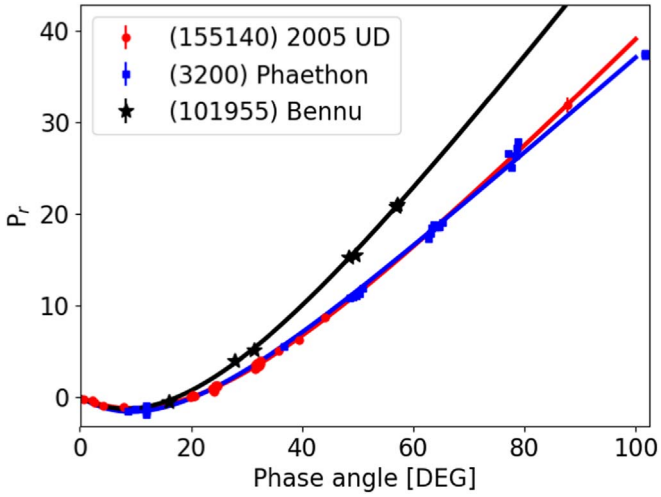

Figure 5. Comparison of the phase-polarization curves for three B-type asteroids: 2005 UD (red circles; this work), Phaethon (blue squares; Devogèle et al. 2018; Ito et al. 2018; Shinnaka et al. 2018), and (101955) Bennu (black stars; Cellino et al. 2018). The continuous curves correspond to a fit of the exponential-linear model to the respective data. The Phaethon and UD polarization curves are almost identical while strongly differing from that of Bennu, another B-type asteroid. Error bars are included for each measurement but are generally smaller than the symbols.

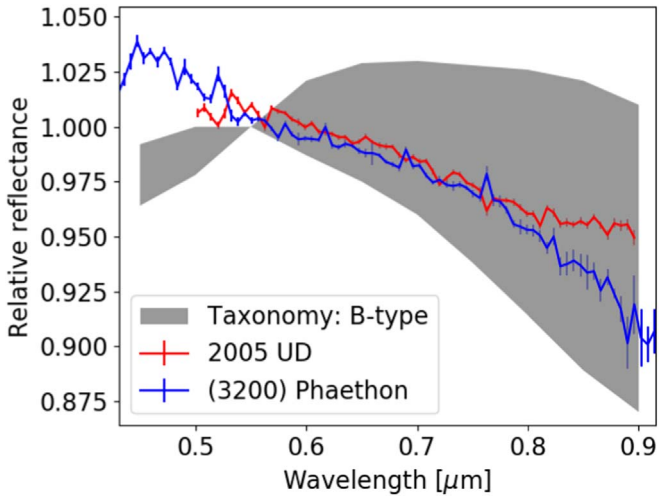

Figure 6. Comparison of the spectra of 2005 UD, Phaethon, and the B-type template from the Bus-Demeo system.

3.6. Taxonomic Classification

Our average visible (0.5–0.9 μm) spectrum of UD, normalized at 0.55 μm, is shown in Figure 6. The UD spectrum displays an almost constant blue slope long-ward of 0.6 μm with a maximum reflectance around 0.55 μm typical of B-type asteroids in the Bus-DeMeo classification system (DeMeo et al. 2009). Even if the spectrum of UD does not seem to follow the envelope of the B-type in the Bus-DeMeo taxonomy, we note that in the Bus and Binzel taxonomy (Bus & Binzel 2002), a change in slope below 0.55 μm is not present, and the B-type envelope traces a continuous blue slope from 0.44 to 0.92 μm as observed for UD. Figure 6 also compares the spectrum of UD to that of Phaethon. They appear to be almost identical except for the longest wavelengths, where the spectrum of Phaethon is slightly bluer. Slope variation for B-type asteroids has been linked to the degree of hydration. B-types display a range of slopes at near-infrared wavelengths (0.9–2.5 μm) that include both negative and positive values. Red (positive) sloped B-types are spectrally consistent with hydrous carbonaceous chondrites, while blue (negative) sloped asteroids are consistent with dry, thermally metamorphosed chondrites (de Leon et al. 2012). However, blue-sloped (101955) Bennu was found by the OSIRIS-REx spacecraft to have significant amounts of hydrous material (Hamilton et al. 2019). Even though our spectra only cover visible wavelengths, the difference in slope between UD and Phaethon at the red end of the spectra, if attributable to a physical difference in surface properties, could be due to differences in the degree of thermal alteration or hydration state.

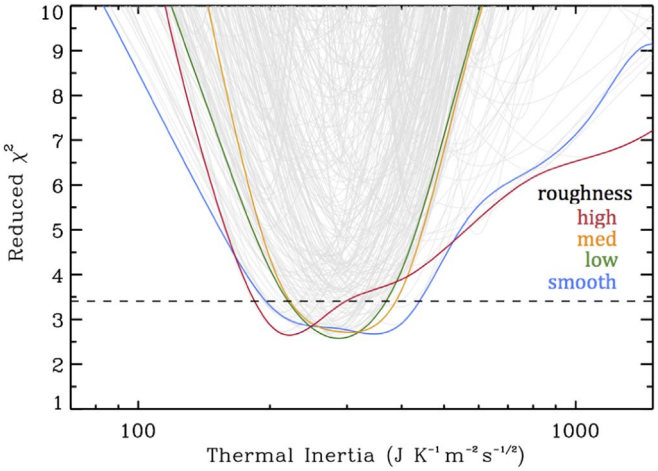

Figure 7. Reduced χ^2 best-fit TPM curves as a function of thermal inertia. Each gray curve represents a set of model fits for a given spin axis and roughness value, after the best-fit diameter has been determined. Colored curves encompass the default roughness values, as indicated on the figure.

3.7. Size and Thermal Inertia

Using the NEOWISE-R observations and TPM, we are able to place constraints on the size, albedo, thermal inertia, and spin axis of UD. Figure 7 shows TPM reduced χ^2 best-fit curves as a function of thermal inertia for different sets of pole orientation and surface roughness values. It shows that the surface rough could not be constrained, most likely due to the fact that the object was observed at such large phase angles. As depicted in Figure 1 of MacLennan & Emery (2018), the color temperature is largely unaffected by surface topography when an object is observed at phase angles approaching 60°. A summary of our TPM fits is given in Table 4. The diameter and albedo values closely match those reported in Masiero et al. (2019), who used the same data set but a different TPM approach. The thermal inertia of 300^{+120}_{-110} J m^{-2} K^{-1} s$^{-1/2}$ is approximately half that of the estimates for Phaethon (600 ± 200 and 800 J m^{-2} K^{-1} s$^{-1/2}$; Hanuš et al. 2016; Masiero et al. 2019, respectively), although there is partial overlap when 1σ uncertainties are considered.

3.8. Thermal Grain Size Estimates

Using the thermal inertia derived above, we estimate thermal grain sizes of the surface regolith for UD following the methods outlined in Gundlach & Blum (2013).

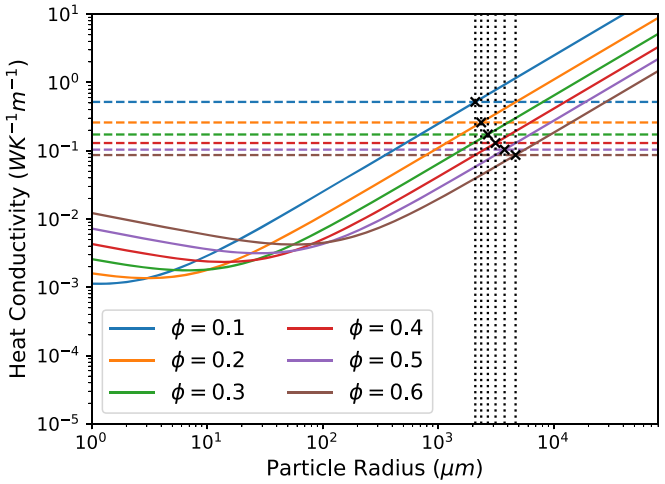

Figure 8. Heat conductivity plotted against particle radius of the surface regolith for UD. Heat conductivities derived from the mean thermal inertia ($\Gamma = 300$) and mean heliocentric distance ($r = 1.2$ au) are shown as dashed lines. Heat conductivites derived using the heat conductivity model for regolith in a vacuum using carbonaceous-rich meteorite analogs (Gundlach & Blum 2013) are shown as the solid curved lines. The derived grain size estimates (crosses with vertical dotted lines) are in the range 2–4.6 mm.

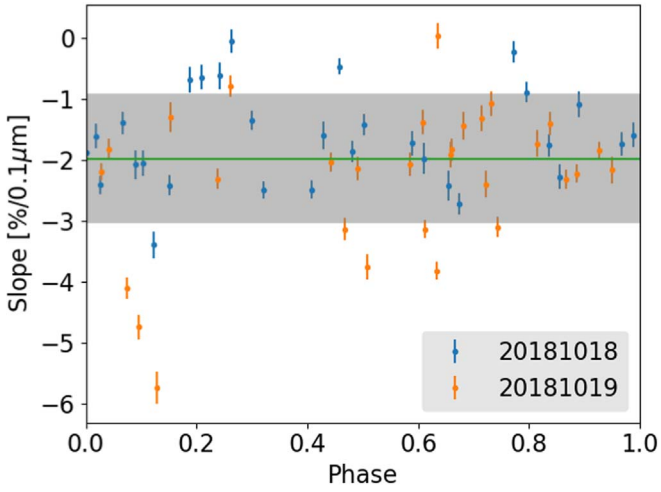

Figure 9. Spectral slope of UD between 0.65 and 0.85 μm as a function of rotational phase angle over two consecutive nights. The gray shaded area corresponds to a 1σ deviation of all of the slope measurements, setting a lower limit for any spectral variation that could be detected. No correlated variation of the slope with rotational phase is seen.

We first solve for the heat conductivity of the regolith (λ) using the thermal inertia

$$\Gamma = \sqrt{\lambda C} \tag{3}$$

where C is the volumetric heat capacity ($C = \phi\rho c$) with packing fractions, ϕ, mass density ρ, and specific heat capacity c. We explore a range of values for the packing fraction from 0.1 to 0.6 and adopt a mass density $\rho_C = 3110$ kg m^{-3} and specific heat capacity $c_C(T = 200\,\mathrm{K}) = 560$ J kg^{-1} K^{-1} for carbonaceous chondrite meteorites Cold Bokkeveld and NWA 5515 from Opeil et al. (2010, Table 1; Gundlach & Blum 2013).

The heat conductivity derived from the thermal inertia (Equation (3)) is compared to a model of heat conductivity for regolith in a vacuum given by $\lambda(r, T, \phi)$, where r is the grain size of the regolith, from Gundlach & Blum (2013) and shown in Figure 8. We again assume carbonaceous material and adopt a value for the heat conductivity $\lambda_{\mathrm{solid},C}(T)$ defined by the meteorites Cold Bokkeveld and NWA 5515. Using the albedo (derived below in Section 4.3), the thermal inertia, and surface temperature, we estimate a range of grain sizes for the regolith of UD.

Figure 8 shows an example of grain size estimates for UD using a mean thermal inertia ($\Gamma = 300$) and temperature ($T = 343 \pm 18$ K) derived from the blackbody fit to the thermal data plotted as the derived heat conductivity using the two methods described above for different particle radii from 1 μm to 100 mm. The heat conductivities derived at different packing fractions of ϕ from 0.1 to 0.6 are shown as the dashed lines, while the heat conductivities derived at different packing fractions using the heat conductivity model for regolith in a vacuum are shown as the solid curved lines. The resulting grain size estimates from this specific thermal inertia (crosses with dotted vertical lines) are in the range 2–4.6 mm. Considering the full range of thermal inertia values within one standard deviation, we derive grain size estimates for UD in the range of 0.9–10 mm.

3.9. Surface Homogeneity

Rotational variation of UD's photometric colors has been reported by Kinoshita et al. (2007). To probe for surface variations as a function of rotation, we continuously observed UD for intervals longer than one rotation period in both spectroscopy and polarimetry.

Since the visible spectrum of UD is largely featureless and shows a uniform slope, we used slope as a diagnostic metric to search for correlation with rotation. We obtained a linear fit to the spectra between 0.65 and 0.85 μm using the SciPy "curve fit" routine. Figure 9 shows the spectral slope of UD between 0.65 and 0.85 μm as a function of the rotation phase ($P = 5.235$ hr). The error bars correspond to the uncertainties of the linear fit to the spectral data. The observed variation of the slope as a function of rotational phase is interpreted as being due to systematic errors (likely introduced during the solar analog correction process), which are not properly accounted for in the error bars. We find that the spectral slope between 0.65 and 0.85 μm is equal to 20 $\pm$ 10% μm^{-1} and that UD does not display any spectral heterogeneity that repeats with rotation phase at a level greater than 10% μm^{-1}.

Similar rotationally resolved observations were attempted in polarimetry. In order to compare data obtained at different phase angles, we divided each observation by the phase-polarization curve model derived in Section 3.5. The observations were phased according to the rotation period ($P = 5.235$ hr) determined in Section 3.1. Figure 10 represents the relative polarization as a function of the rotation phase for UD. Due to a lower absolute polarization value during the second night, the relative error bar on the polarization measurement is higher than that for the first night. The second night thus sets the lower limit on polarization variation possibly detectable to be around 16%. We do not detect any variation of the polarization of UD correlated with rotational phase at that level or higher. 2005 UD was much fainter and was observed at a lower phase angle than corresponding observations of Phaethon for which rotational variation of the polarization of the order of 3% was reported (Borisov et al. 2018). As a consequence, these observations cannot rule out polarization variation at the same level as those observed for Phaethon.

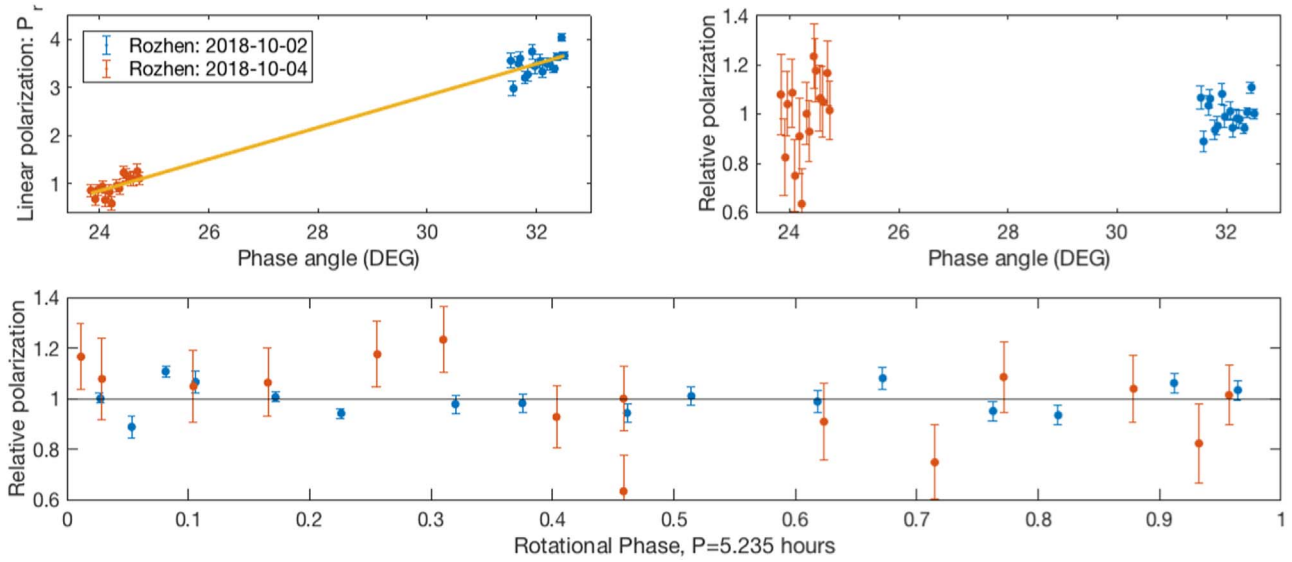

Figure 10. Top left panel: phase-polarization curve of 2005 UD. The yellow line corresponds to a fit of the data using the linear exponential model (Muinonen et al. 2009). Top right panel: relative polarization of UD (i.e., the phase-polarization curve of UD divided by the linear exponential model). Lower panel: relative polarization of UD phased according to the rotation period determined in this work ($P = 5.235$ hr).

4. Discussion

4.1. Are Phaethon and 2005 UD Related?

Our observations of UD suggest that it displays similar physical properties as Phaethon in both spectroscopy and polarimetry. UD and Phaethon are taxonomically classified as B-types, which are rare. In various surveys, their observed abundance ranges from 0.68% to 2.8% of the NEO population (Perna et al. 2018; Binzel et al. 2019; Devogèle et al. 2019). Based on the abundance of B-type NEOs, the probability to randomly draw two B-types from the NEO population is no greater than 0.08% (taking into account the 2.8% abundance). However, two randomly drawn asteroids will also have random orbits. Computing the probability of drawing two B-types with similar orbits is beyond the scope of this paper. Moreover, the similarities between Phaethon and UD is even stronger than just being classified as B-types. As seen in Figure 5, the phase-polarization curves of Phaethon and UD cannot be distinguished for those phase angles at which we have simultaneous coverage. However, both differ from the phase-polarization curve of (155140) Bennu, another B-type asteroid (Cellino et al. 2018). Namely, the phase-polarization curve of Bennu displays higher polarization than Phaethon and UD. The similarities between UD and Phaethon are not sufficient per-se to definitively state that they are genetically related but provide strong evidence for such a relationship even if they do not meet dynamical criteria to be formally linked (Ryabova et al. 2019).

4.2. Photometric Phase Curves of Phaethon and UD

Several photometric phase curves have been published for Phaethon (Ansdell et al. 2014; Tabeshian et al. 2019). However, the phase coverages obtained for UD and Phaethon have been very different. In the case of Phaethon, there exist no observations at phase angles $\alpha < 12°$, thus, preventing determination of the opposition surge and leading to uncertainties on determination of its H magnitude. On the other hand, the phase coverage for Phaethon extends to phase angles as high as $\alpha = 100°$. In the case of UD, we have phase coverage down to very small angles ($\alpha = 0.^{\circ}7$) allowing for a precise determination of the opposition surge and the H absolute magnitude, but the maximum observed phase angle, in photometry, is only $\alpha = 58°$.

If we assume that Phaethon and UD are related and that their surface properties are identical, we can directly compare their photometric phase curves by applying a magnitude offset. In the case of Phaethon, Ansdell et al. (2014) reported observations of Phaethon between 12° and 83° of phase angle and analyzed the photometric phase curve using the H, G system (Bowell et al. 1989). They report values of $H_V = 13.9$ mag and $G = 0.06$. Tabeshian et al. (2019) reported observations of Phaethon for phase angles of 20° to 100° and reported $H_R = 13.28$ mag (yielding $H_V = 13.63$ assuming solar V–R color), and $G = -0.10$. Tabeshian et al. (2019) computed the phase curve of Phaethon in the B, V, R, and I filters. We considered here their measurements in the R filter, as they are closest to our observations. Both of these phase curves presume an opposition surge of ∼0.4 mag at phase angles for which no data are available. This seems inconsistent with the phase curve of UD presented here (see Figure 4), which shows very little to no opposition surge.

In Figure 11, we compared the phase curve of UD obtained in this work with the offset phase curves of Phaethon derived by Ansdell et al. (2014) and Tabeshian et al. (2019). The offset is computed so as to minimize the difference between the magnitudes at those phase angles for which both UD and Phaethon have observations (12°–58° and 20°–58° for Ansdell et al. 2014 and Tabeshian et al. 2019, respectively). We can see that in both cases, the lack of observations for Phaethon at small phase angles results in phase curves that are offset toward smaller H relative to the phase curve, which would be expected if UD and Phaethon displayed identical photometric properties. These offsets of 0.11 Ansdell et al. (2014) and 0.53 Tabeshian et al. (2019) magnitude can result in over-estimation of the diameter by up to ∼20% (considering a fixed albedo) or an under-estimation of the albedo of up to ∼50% (considering a fixed diameter).

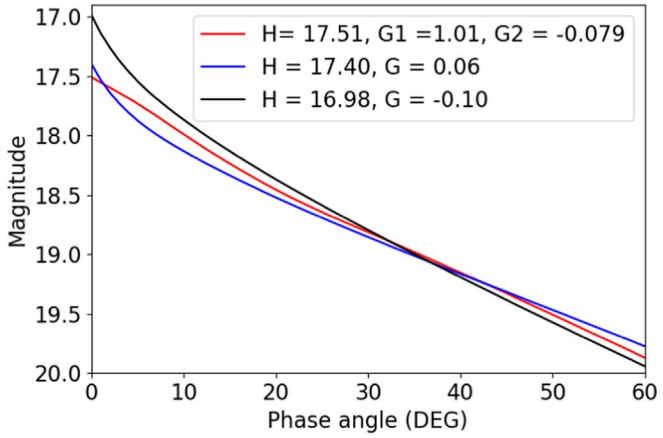

Figure 11. Phase-curve models with different parameters. The red curve represents the modeled phase curve of UD using the H, G_1, and G_2 model. The blue and black curves represent models of the phase curve of Phaethon with an offset to match the one of UD. Both of Phaethon's phase curve are characterized with a strong opposition surge (although no data have ever been observed at those phase angles), while this surge is absent in the case of UD (for which data at very small angles are available).

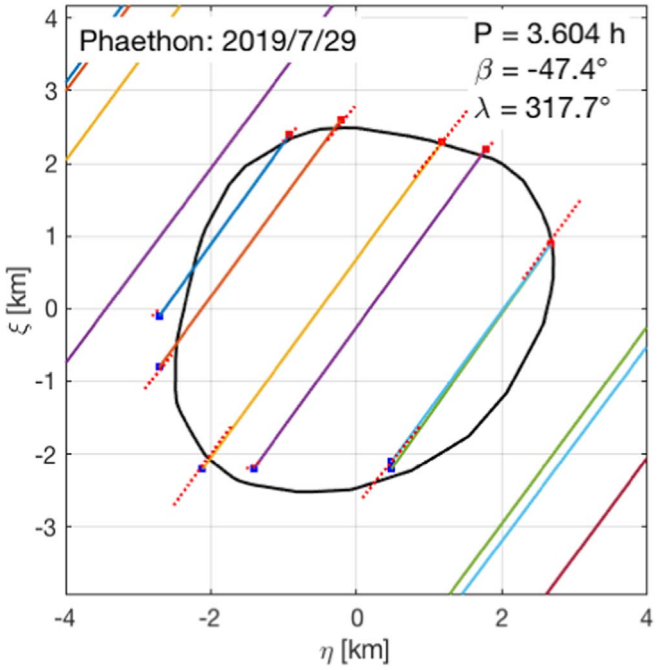

Figure 12. Fit of the sky-projected silhouette of the shape model of Phaethon on the occultation chords observed on 2019 July 29 Dunham et al. (2019). The best-fit solution suggests a diameter $D = 5.2 \pm 0.1$.

4.3. Albedo and Size of Phaethon and UD

We use the albedo–polarization relation (Cellino et al. 2015) and TPM to obtain independent estimates of the albedo of UD and Phaethon. Cellino et al. (2015) proposed two relations depending on albedo with a threshold around $p_V = 0.08$. Unfortunately, the albedo of UD and Phaethon is close to that threshold, and the two relations provide quite different values. Considering the slope of the polarimetric phase curve at the inversion angle ($h = 0.22 \pm 0.01\%/^\circ$) and using the high-albedo relation, we obtain a polarimetric albedo of $p_V = 0.11 \pm 0.02$. On the other hand, using the low-albedo relation provides an albedo of $p_V = 0.09 \pm 0.02$. Thermophysical modeling provides higher values for the albedo ($p_v = 0.14 \pm 0.07$), as detailed in Section 3.7. As these values are all consistent within 1σ, we adopt an albedo for UD to be the weighted average from the different techniques $p_v = 0.10 \pm 0.02$.

We saw, in Section 1 and throughout this work, that, for both UD and Phaethon, independent techniques provide an inconsistent determination of the size and/or albedo. Considering the albedo determined in the last paragraph and considering that Phaethon and UD have similar inferred surface properties, we can derive new estimates for the sizes of the two objects. Taking the H_V magnitude for Phaethon reported by Tabeshian et al. (2019) and taking into account the offset found in Section 4.2, we find that the H magnitude of Phaethon can be revised to $H = 14.2$ mag. This computed H implies a size of 6.1 ± 0.7 km assuming $p_v = 0.10 \pm 0.02$. Taylor et al. (2019) measured, via Doppler delay radar imaging, an equatorial diameter of 6.2 km, consistent with our inferred size.

Another estimation of the size of Phaethon can also be obtained via stellar occultation data (Dunham et al. 2019). We fit the sky-projected silhouette of the Hanuš et al. (2018) shape model of Phaethon to the observed extremes of the occultation chords by scaling the light-curve-derived shape model to a best-fit size. Figure 12 represents the best fit of the shape model of Phaethon to occultation chords observed on 2019 July 29 (Dunham et al. 2019). Details about the fitting procedure can be found in Devogèle et al. (2017). Our estimated occultation-derived diameter for Phaethon is $D = 5.2 \pm 0.1$ km. This estimation seems to be smaller than those of either the radar or photometric estimations. However, the largest axis of Phaethon based on the occultation and the Hanuš et al. (2018) shape model is estimated to be $a = 6.1$ km, which agrees with the equatorial diameter observed using the radar technique.

In the case of UD, considering the albedo $p_v = 0.10 \pm 0.02$ and $H_V = 17.51 \pm 0.02$ derived in this work, we obtain a diameter of 1.3 ± 0.2 km. Both of these values are in agreement with Masiero et al. (2019), who suggest $D = 1.2 \pm 0.4$ km and $p_V = 0.14 \pm 0.09$.

4.4. Regolith Properties of Phaethon and UD

From the derived thermal inertia for UD, and following the method laid out by Gundlach & Blum (2013), we estimated surface grain sizes in the range of 0.9–10 mm. Using the same technique, we update grain size estimates for Phaethon using the new albedo ($p_v = 0.10$) determined above. We find grain size estimates for Phaethon in the range of 3–30 mm, slightly larger than those for UD. Gundlach & Blum (2013) report thermal grain size estimates for Pallas, the suspected parent member of Phaethon (de León et al. 2010; Todorović 2018), of $9.2^{+27.8}_{-0.0}$ μm, which are finer than the approximately millimeter grain size estimates we find for UD. Coarser surface grains on UD in comparison to Pallas are consistent with our expectation that larger bodies have finer regolith (e.g., Delbo' et al. 2007; Hanuš et al. 2018). However, the grain size trend does not hold for UD and Phaethon, where Phaethon is larger in size yet may also have larger surface grains.

We present three possible mechanisms that could explain this discrepancy: (1) Phaethon could have a high thermal inertia due to retention of coarse grains and removal of small particles during mass ejection events at perihelion (Jewitt et al. 2013), (2) as an active body, mass movement on the surface could lead to size sorting and preferential exposure of coarser subsurface

material, and (3) Phaethon, like Bennu, could be covered in boulders. Rozitis et al. (2019) find two types of boulders on Bennu—low thermal inertia boulders and high thermal inertia boulders. With Phaethon's activity proposed to be a result of thermal fracture (Jewitt & Li 2010), we suggest the possibility that the low thermal inertia boulders are weaker and disrupted near perihelion, leaving the surface covered in only high thermal inertia boulders.

Another possibility is that UD does not fit expectations due to a lower-than-expected thermal inertia. We present two possible explanations for this: (1) UD may be covered in low thermal inertia boulders as observed on Ryugu (Grott et al. 2019) and Bennu (Dellagiustina et al. 2019) leading to a structural influence on thermal inertia rather than the result of grain size effects, and (2) UD may have undergone faster rotation in its past, which could have removed large particles from its surface such that only fine grains held together by van der Waal forces would be left behind, analogous to what is hypothesized for 1950 DA (Rozitis et al. 2014).

5. Conclusion

We obtained photometric, spectroscopic, and polarimetric observations of the asteroid 2005 UD, a potential genetically related pair to (3200) Phaethon. We also reanalyzed thermal-IR data of UD from the NEOWISE-R mission. These observations allowed for a detailed characterization of UD's physical properties and a comparison to those of Phaethon.

Spectroscopic and polarimetric observations of UD display similar characteristics to those of Phaethon. These include rare spectroscopic (B-type) and polarimetric (high-polarization) signatures, which is a strong indication that these asteroids are in fact genetically related.

The photometric observations allowed us to constrain the spin properties of UD. We report a sidereal rotation period of $P = 5.235 \pm 0.005$ hr. The light curves observed over the whole apparition are symmetric, with a reduced amplitude at a zero phase angle of $Am(0) = 0.29$ mag and increase at a rate of $m = 0.017$ mag per degree of phase angle. The large range of phase angles accessed with our observations allowed for the derivation of the photometric parameters of UD in the H, G_1, and G_2 system. We find $H_V = 17.51 \pm 0.02$ mag, $G_1 = 1.09 \pm 0.02$, and $G_2 = -0.10 \pm 0.01$.

A search for the pole orientation of UD did not provide a unique solution, but large areas of that parameter space could be excluded. Our search for pole orientation using two independent data sets led to similar results, with a pole solution most likely located around ecliptic latitude and longitudes of $(90° \pm 30°, 0° \pm 50°)$ or $(-90° \pm 30°, 0° \pm 50°)$. A pole solution similar to the one of Phaethon ($\lambda = -46°$, $\beta = -47°$, Hanuš et al. 2018) cannot be ruled out, but seems less likely.

A search for surface heterogeneity was also conducted by continuously observing UD in spectroscopy and polarimetry over multiple rotation periods. No variation, correlated with rotation phase greater than 10% μm^{-1} in spectral slope and 16% in polarization ratio, was observed.

The polarization measurement allowed us to determine a reliable phase-polarization curve for UD. We found that the polarization measurements obtained for Phaethon are fully consistent with those of UD and that Phaethon and UD can be modeled using a single phase-polarization curve. Using the polarization-albedo relation, we found that the albedo of UD could either be $p_v = 0.11 \pm 0.02$ or $p_v = 0.09 \pm 0.02$ depending on the adopted relationship.

NEOWISE thermal infrared observations of UD allowed us to obtain constraints on the thermal inertia $\Gamma = 300^{+120}_{-110}$, albedo $p_v = 0.14 \pm 0.07$, and diameter $D = 1.12^{+0.49}_{-0.21}$. Using the new albedo and thermal inertia measurements, we estimated the surface grain sizes for Phaethon and UD. Our predictions indicate that Phaethon may have coarser surface regolith than UD, and we provide some possible scenarios to explain why this may be.

We gratefully acknowledge observing grant support from the Institute of Astronomy and Rozhen National Astronomical Observatory, Bulgarian Academy of Sciences. Based on data collected with 2 m RCC telescope at Rozhen National Astronomical Observatory. Based on observations obtained at the Southern Astrophysical Research (SOAR) telescope, which is a joint project of the Ministério da Ciência, Tecnologia, Inovações e Comunicações (MCTIC) do Brasil, the U.S. National Optical Astronomy Observatory (NOAO), the University of North Carolina at Chapel Hill (UNC), and Michigan State University (MSU). The data presented here were obtained in part with ALFOSC, which is provided by the Instituto de Astrofisica de Andalucia (IAA) under a joint agreement with the University of Copenhagen and NOTSA. TRAPPIST is a project funded by the Belgian Fonds (National) de la Recherche Scientifique (F.R.S.-FNRS) under grant FRFC 2.5.594.09.F. TRAPPIST-North is a project funded by the University of Liège, in collaboration with the Cadi Ayyad University of Marrakech (Morocco). E.J. is an FNRS Senior Research Associate. M.G., G.F., L.S., M.P., and E.M. acknowledge funding from the Academy of Finland. Based on observations made with the Nordic Optical Telescope, operated by the Nordic Optical Telescope Scientific Association at the Observatorio del Roque de los Muchachos, La Palma, Spain, of the Instituto de Astrofisica de Canarias. D.P. is grateful to the Wise Observatory staff for their ongoing support. The authors acknowledge support from NASA NEOO grants NNX14AN82G, and NNX17AH06G. The authors are greateful to the observers of the stellar occultation of Phaethon (J. Bardecker, K. Bender, D. Blanchette, J. Briggs, M. Buie, K. Caceres, K. Cobble, S. Degenhardt, D. Dunham, J. Dunham, K. Getrost, R. Howard, J. Jewell, R. Jones, B. Keeney, J. Keller, W. Kloepping, J. Kok, R. Leiva, G. Lyzenga, F. Marchis, W. Merline, J. Moore, R. Nolthenius, A. Parker, S. Preston, R. Royer, J. Salmon, L. Sherade, D. Terrell, W. Thomas, A. Vebiscer, B. Whitehurst, E. Wilson, Q. Ye, and Q. Zhang).

ORCID iDs

Maxime Devogèle https://orcid.org/0000-0002-6509-6360
Annika Gustafsson https://orcid.org/0000-0002-7600-4652
Nicholas Moskovitz https://orcid.org/0000-0001-6765-6336
Mikael Granvik https://orcid.org/0000-0002-5624-1888
Michael Mommert https://orcid.org/0000-0002-8132-778X
Fumi Yoshida https://orcid.org/0000-0002-3286-911X

References

Alí-Lagoa, V., de León, J., Licandro, J., et al. 2013, A&A, 554, A71
Ansdell, M., Meech, K. J., Hainaut, O., et al. 2014, ApJ, 793, 50
Arai, T., Kobayashi, M., Ishibashi, K., et al. 2018, LPI, 49, 2570
Babadzhanov, P., & Obrubov, I. V. 1987, PAICz, 67, 141

Bagnulo, S., Boehnhardt, H., Muinonen, K., et al. 2006, A&A, 450, 1239
Belskaya, I., & Shevchenko, V. 2000, Icar, 147, 94
Binzel, R., DeMeo, F., Turtelboom, E., et al. 2019, Icar, 324, 41
Borisov, G., Devogèle, M., Cellino, A., et al. 2018, MNRAS, 480, L131
Bowell, E., Hapke, B., Domingue, D., et al. 1989, in Proc. Asteroids II Conf., ed. R. P. Binzel, T. Gehrels, & M. S. Matthews (Tucson, AZ: Univ. Arizona Press), 524
Brosch, N., Kaspi, S., Niv, S., & Manulis, I. 2015, Ap&SS, 359, 49
Bus, S. J., & Binzel, R. P. 2002, Icar, 158, 146
Cellino, A., Bagnulo, S., Belskaya, I., & Christou, A. 2018, MNRAS, 481, L49
Cellino, A., Bagnulo, S., Gil-Hutton, R., et al. 2015, MNRAS, 455, 2091
Christensen, E. J., Beshore, E. C., Garradd, G. J., et al. 2005, 2005 UD, Tech. Rep. MPEC 2005-U22 (Cambridge, MA: Minor Planet Center), https://minorplanetcenter.net//mpec/K05/K05U22.html
Cutri, R. 2012, yCat, 2311
Delbo', M., dell'Oro, A., Harris, A. W., Mottola, S., & Mueller, M. 2007, Icar, 190, 236
de León, J., Campins, H., Tsiganis, K., Morbidelli, A., & Licandro, J. 2010, A&A, 513, A26
de Leon, J., Pinilla-Alonso, N., Campins, H., Licandro, J., & Marzo, G. 2012, Icar, 218, 196
Dellagiustina, D. N., Emery, J. P., Golish, D. R., et al. 2019, NatAs, 3, 341
DeMeo, F. E., Binzel, R. P., Slivan, S. M., & Bus, S. J. 2009, Icar, 202, 160
Devogèle, M., Cellino, A., Christou, A., et al. 2018, MNRAS, 479, 3498
Devogèle, M., Moskovitz, N., Thirouin, A., et al. 2019, AJ, 158, 196
Devogèle, M., Tanga, P., Bendjoya, P., et al. 2017, A&A, 607, A119
Dunham, D. W., Dunham, J. B., Buie, M., et al. 2019, LPICo, 2189, https://www.hou.usra.edu/meetings/asteroidscience2019/pdf/2062.pdf
Gould, B. 1855, AJ, 4, 81
Granvik, M., Morbidelli, A., Jedicke, R., et al. 2016, Natur, 530, 303
Grott, M., Knollenberg, J., Hamm, M., et al. 2019, NatAs, 3, 971
Gundlach, B., & Blum, J. 2013, Icar, 223, 479
Hamilton, V., Simon, A., Christensen, P., et al. 2019, NatAs, 3, 332
Hanuš, J., Delbo, M., Vokrouhlicky`, D., et al. 2016, A&A, 592, A34
Hanuš, J., Ďurech, J., Brož, M., et al. 2011, A&A, 530, A134
Hanuš, J., Ďurech, J., Brož, M., et al. 2013, A&A, 551, A67
Hanuš, J., Vokrouhlicky`, D., Delbo, M., et al. 2018, A&A, 620, L8
Hapke, B. 1984, Icar, 59, 41
Harris, A., Pravec, P., Galád, A., et al. 2014, Icar, 235, 55
Holmberg, J., Flynn, C., & Portinari, L. 2006, MNRAS, 367, 449
Ito, T., Ishiguro, M., Arai, T., et al. 2018, NatCo, 9, 2486
Jakubík, M., & Neslušan, L. 2015, MNRAS, 453, 1186
Jehin, E., Gillon, M., Queloz, D., et al. 2011, Msngr, 145, 2
Jewitt, D., & Hsieh, H. 2006, AJ, 132, 1624
Jewitt, D., & Li, J. 2010, AJ, 140, 1519
Jewitt, D., Li, J., & Agarwal, J. 2013, ApJL, 771, L36
Jockers, K., Credner, T., Bonev, T., et al. 2000, KFNTS, 3, 13
Jordi, K., Grebel, E. K., & Ammon, K. 2006, A&A, 460, 339
Kaasalainen, M. 2004, A&A, 422, L39
Kaasalainen, M., & Torppa, J. 2001, Icar, 153, 24
Kaasalainen, M., Torppa, J., & Muinonen, K. 2001, Icar, 153, 37
Kareta, T., Reddy, V., Hergenrother, C., et al. 2018, AJ, 156, 287
Kasuga, T., & Jewitt, D. 2008, AJ, 136, 881
Kinoshita, D., Ohtsuka, K., Sekiguchi, T., et al. 2007, A&A, 466, 1153
Li, J., & Jewitt, D. 2013, AJ, 145, 154
MacLennan, E. M., & Emery, J. P. 2018, AJ, 157, 2
Mainzer, A., Bauer, J., Cutri, R., et al. 2014, ApJ, 792, 30
Mainzer, A., Bauer, J., Grav, T., et al. 2011, ApJ, 731, 53
Masiero, J. R., Wright, E., & Mainzer, A. 2019, AJ, 158, 97
Mommert, M. 2017, A&C, 18, 47
Muinonen, K., Belskaya, I. N., Cellino, A., et al. 2010, Icar, 209, 542
Muinonen, K., Penttilä, A., Cellino, A., et al. 2009, M&PS, 44, 1937
Ohtsuka, K., Arakida, H., Ito, T., Yoshikawa, M., & Asher, D. 2008, M&PSA, 43, 5055
Ohtsuka, K., Sekiguchi, T., Kinoshita, D., et al. 2006, A&A, 450, L25
Ohtsuka, K., Sekiguchi, T., Kinoshita, D., & Watanabe, J. 2005, CBET, 283
Opeil, C. P., Consolmagno, G. J., & Britt, D. T. 2010, Icar, 208, 449
Peirce, B. 1852, AJ, 2, 161
Penttilä, A., Shevchenko, V., Wilkman, O., & Muinonen, K. 2016, P&SS, 123, 117
Perna, D., Barucci, M. A., Fulchignoni, M., et al. 2018, P&SS, 157, 82
Polishook, D., & Brosch, N. 2009, Icar, 199, 319
Pravec, P., Vokrouhlicky`, D., Polishook, D., et al. 2010, Natur, 466, 1085
Rozitis, B., Emery, J., Ryan, A., et al. 2019, EPSC, 13, 548
Rozitis, B., Green, S., MacLennan, E., & Emery, J. 2018, MNRAS, 477, 1782
Rozitis, B., Maclennan, E., & Emery, J. P. 2014, Natur, 512, 174
Ryabova, G. 2012, MNRAS, 423, 2254
Ryabova, G., Avdyushev, V., & Williams, I. 2019, MNRAS, 485, 3378
Schunová, E., Jedicke, R., Walsh, K. J., et al. 2014, Icar, 238, 156
Shinnaka, Y., Kasuga, T., Furusho, R., et al. 2018, ApJL, 864, L33
Shurcliff, W. 1962, Polarized Light: Production and Use (Cambridge, MA: Harvard Univ. Press)
Tabeshian, M., Wiegert, P., Ye, Q., et al. 2019, AJ, 158, 30
Taylor, P. A., Rivera-Valentin, E. G., Benner, L. A., et al. 2019, P&SS, 167, 1
Todorović, N. 2018, MNRAS, 475, 601
Whipple, F. L. 1983, IAUC, 3881
Wright, E. L., Eisenhardt, P. R., Mainzer, A. K., et al. 2010, AJ, 140, 1868
Zappala, V., Cellino, A., Barucci, A., Fulchignoni, M., & Lupishko, D. 1990, A&A, 231, 548
Zheltobryukhov, M., Chornaya, E., Kochergin, A., et al. 2018, A&A, 620, A179